ETH
Eidgenössische Technische Hochschule Zürich
Swiss Federal Institute of Technology Zurich

ETH Institute for Particle Physics

Radiation Effects on the CMS Silicon Pixel Modules during LHC Run 1

Semester Thesis

July 29, 2014

Myriam Schönenberger

Advisors: Prof. Dr. R. Wallny, Dr. A. Starodumov
Collaborator: Dr. M. Takahashi
Institute for Particle Physics
ETHZ

Version 3 (not final)

The eight CMS pixel modules were examined for their behavior after irradiation with approximately $2.4{\cdot}10^{13}\frac{1}{\mathrm{cm}^2}$ 1 MeV neutron equivalent fluence during LHC Run 1. Namely 3 changes compared to the calibration conducted in 2008 are discussed: the parameters that control the readout electronics, the leakage current of the silicon sensor and the calibration of the particle signal detected.

After irradiation changes in the optimum values of the following readout parameters were observed compared to 2008: VIbias_DAC, VOffsetOp, Vana, VcThr, Vsf and VIbias_PH. CalDel and Vtrim remained on average unchanged. These shifts can only partially be explained by the change of the reference voltage to which all voltages are compared and which is know to change with irradiation.

The leakage current increased as expected and using the fluence predicted by the detailed CMS simulation the current related damage rate α was calculated to be on average

$$\alpha_{mean} = 3.86 \pm 0.14 \cdot 10^{-17}\mathrm{A/cm},$$

which corresponds to approximately 1 month of annealing at $21\,^{\circ}$C.

Finally for the calibration of the signal using X-rays an average of 77.6 electrons per readout unit (e^-/VCal) was observed while the corresponding measurements before irradiation in 2008 using a different method was 66.5 e^-/VCal.

Contents

1 Introduction

Even after the discovery of the Higgs particle, or maybe especially because of it, there are still a lot of unanswered questions in particle physics. With the large hadron collider (LHC) achieving a center of mass energy of up to 14 TeV starting 2015 we might have the possibility to answer at least some of them. For such high energies and particle flux suitable detectors had to be built, like the Compact Muon Solenoid (CMS) detector. For the measurements, for example the determination of the Higgs coupling, a high instantaneous luminosity is necessary in order to achieve high enough statistics in a reasonable amount of time. But a high enough statistics means a high particle flux through the detector that will result in a deterioration of the material. Thus radiation hardness is a crucial point for the development of all detectors at the LHC, especially so for the innermost detectors, the pixel detectors.

For the CMS pixel detectors, silicon (Si) is chosen for the active material because of its cost-effectiveness and availability of the raw material but also because of the simple production of very pure silicon wafers due to the advancement of the commercial chip industry. The radiation effects from high energetic particles on the sensor and read out chip were studied during development in oder to predict and anticipate for their effect on the detector performance over the operational period. The goal of this thesis is to assess the changes of the performance of the pixel modules irradiated with a particle fluence of approximately $2.4 \cdot 10^{13} \frac{1}{\mathrm{cm}^2}$ 1 MeV neutron equivalent dose, i.e. approximately $30\,\mathrm{fb}^{-1}$ during LHC Run 1.

Seven of the eight modules that were tested had to be replaced because they would give infinitely long readouts with a probability that increases with the particle rate. This resulted in the fact that they had to be turned off completely in order to not disturb the readout of the other connected modules. The other module just did not work properly anymore. These eight modules were thus extracted from the detector during the shutdown after Run 1 and retested at the ETH under as similar as possible conditions as the calibration done prior to their installment in 2008. This gives the unique opportunity to qualify the changes of the optimum parameter values for the readout electronics, in the leakage current and finally in the amount of charge read out of the sensor after irradiation at P5 at the LHC. These values will be useful for calibrating not only the parameters for the modules still in the detector but also for the simulations.

2 CERN, the LHC and CMS

The most prominent machine of CERN (Conseil Européen pour la Recherche Nucléaire) at the moment is the Large Hadron Collider (LHC) with its four detectors ATLAS (A Toroidal LHC Apparatus), CMS (Compact Muon Solenoid), LHCb (Large Hadron Collider beauty) and ALICE (A Large Ion Collider Experiment). Whereas ATLAS and CMS are all purpose detectors designed to search for what ever new particles and phenomena there might be, LHCb is specialized on b-physics and ALICE is specialized on heavy ion collisions.

In the following an overview of LHC and CMS will be given in order to put the pixel detectors and this work into the bigger context.

2.1 Large Hadron Collider

As the name suggests is the large hadron collider designed to accelerate hadrons, protons and heavy lead ions to be more precise. For the protons the process looks as following: After the electrons are stripped from the hydrogen atom, the thus resulting protons are accelerated by a linear accelerator LINAC2, then the PS Booster injects them in the Proton Synchrotron. Next they are injected into the SPS through which they reach up to 450 GeV until they finally go to the LHC where they are accelerated until they reach the target energy. Figure 2.1 shows the whole accelerator complex and the collision sites at the detectors.

The LHC is designed to circulate protons collected in 2808 bunches with a spacing of 25 ns and $1.1 \cdot 10^{11}$ protons per bunch. In 2012 peak luminosities up to $7.5 \cdot 10^{33}\mathrm{cm}^{-2}\mathrm{s}^{-1}$ at a center of mass energy of $\sqrt{s} = 8\,\mathrm{TeV}$ were reached.

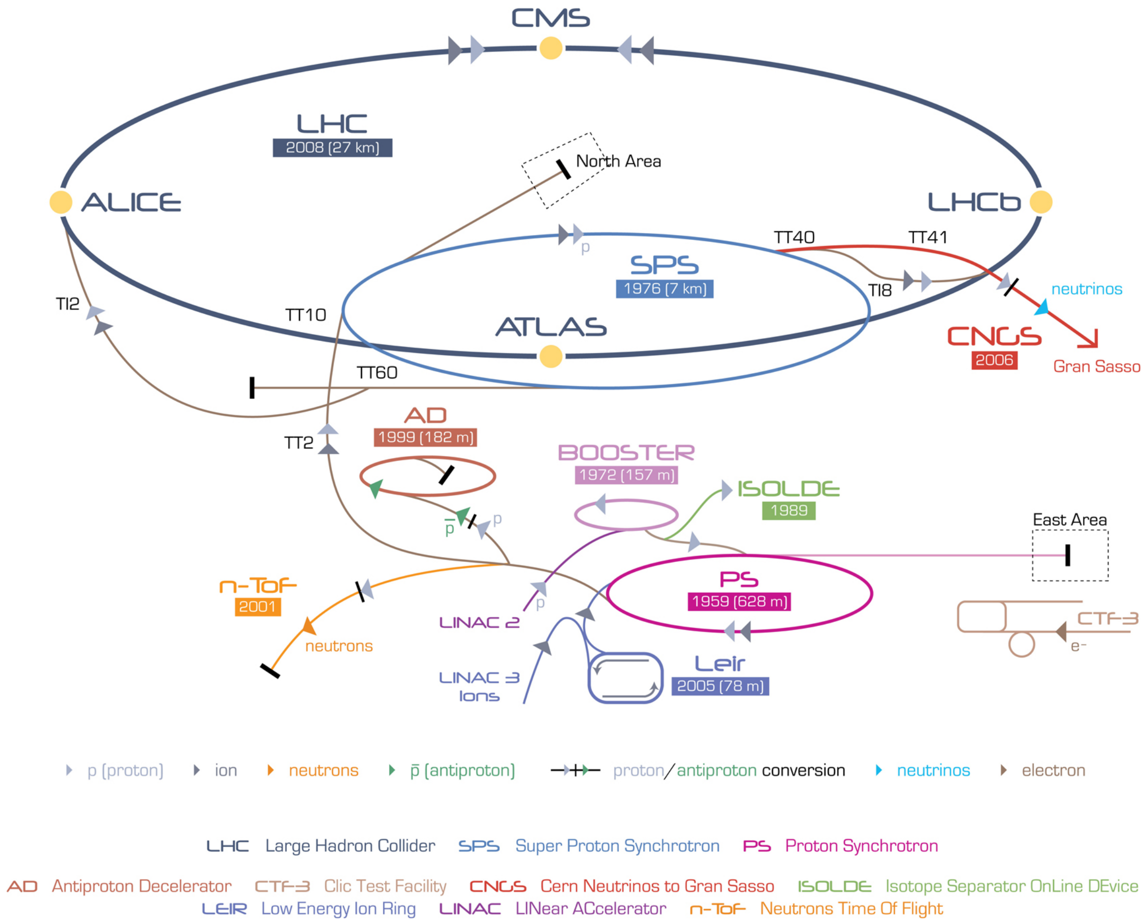

Figure 2.1: The accelerator complex of CERN with the sites of the four detectors [1]

2.2 CMS Detectors

The CMS (Compact Muon Solenoid) detector is a combination of specialized detectors arranged such that it allows for a fast trigger and the vertex, position, energy and particle identification is achieved with the greatest possible accuracy. Because of the symmetry of the colliding beams, CMS has cylindrical symmetry around the beam axis, which is defined as the z-axis of the coordinate system. Another important coordinate is the pseudorapidity $\eta = -\ln\left[\tan\left(\frac{\theta}{2}\right)\right]$, where θ is the angle between the y and the z-axis as shown in Figure 2.2. Each detector type has a barrel and endcap version. Figure 2.3 shows how the different components of the detector are arranged and how particles can be identified by their different energy depositions in the components. A detailed description of the CMS detector can be found in [3].

The different parts of the detector can be distinguished into the following categories:

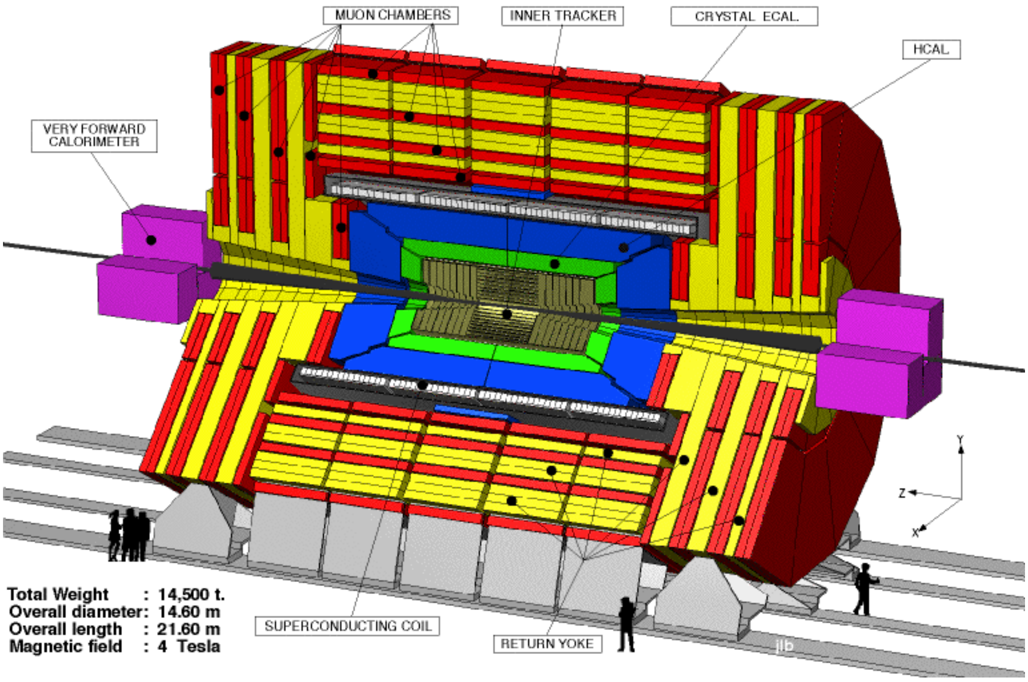

Figure 2.2: Sectional view of the CMS detector with the coordinate axes [2]

Tracker The innermost part of the detector consists of 3 layers of pixel modules in the barrel region and 2 disks in the forward region. The barrel pixel modules are explained in more detail in chapter 3. In the barrel region they are surrounded by 10 layers of silicon strip detectors and in the endcap region by 9 layers. Together they are used to measure the trajectories of charged particles.

ECAL The electromagnetic calorimeter (ECAL) is optimized to read out the energy of electrons, positrons and photons. This is achieved by the use of lead tungstate crystals ($PbWO_4$), 61200 in the barrel region and 7324 in the each of the endcaps. $PbWO_4$ has a short radiation length $X_0 = 0.89\,\text{cm}$, a Moliere radius of 2.2 cm, a fast but low light yield and it is radiation hard.

HCAL Strongly interacting particles, such as protons and pions, are detected in the hadronic calorimeter (HCAL). Because most of the calorimeters are located withing the solenoid, material in terms of interaction lengths had to be maximized. The HCAL was thus chosen to be an inhomogeneous sampling calorimeter with alternating layers of absorber and active material. It consists of Brass as absorber and scintillator tiles as the active material which are read out by wavelength-shifting fibers.

Solenoid The 4 Tesla strong magnetic field is necessary for a good transverse momentum measurement in the tracking system. The solenoid is made of a high-purity aluminium-stabilized superconductor operated at -268.5 $^\circ$C with a current of 20 kA.

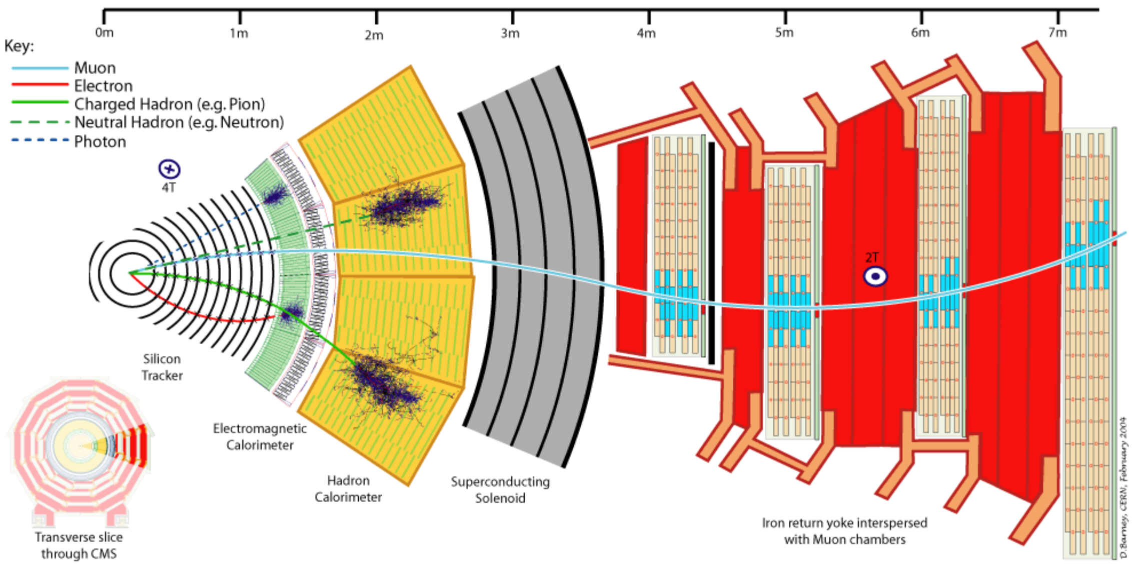

Figure 2.3: The barrel layout of CMS with the track and energy depositions of the different particles in the different detector types [2]

Muon chambers The material and thickness of the previous detector components are choses such that only muons and neutrinos are able to penetrate into the muon chambers. CMS uses three different kinds of gaseous detectors depending on the detector regions and trigger that track the muon: drift tubes chambers, cathode strip chambers and resistive plate chambers.

3 The Barrel Pixel Detector of CMS

The three layers of the barrel pixel detector are at 4.4, 7.3 and 10.2 cm mean distance to the beam axis and are about 53 cm long. In total 768 modules are arranged in half ladders with 4 modules each.

The working principle of a silicon detector is that a charged particle generates electron hole pairs in the doped semiconductor which are collected in the electrodes. The charge deposited in the sensor by a traversing particle is proportional to the amplitude of the signal processed by the readout electronics. This has to be calibrated and is explained in more detail in chapter 6.

The pixel detector has to meet 4 requirements: good spacial resolution, fast readout, radiation hardness and minimal material budget to minimize multiple scattering.

3.1 Pixel Modules

A full pixel module consists of the sensor, which is bump bonded to the readout chips (ROCs) which are in turn connected via wire bonds along the side of the module to the high density interconnect (HDI), which organizes the power supply, signal and trigger informations and the 40 MHz external LHC bunch crossing clock. On the HDI sits the token bit manager (TBM), which coordinates the readout of the ROCs, and the cable connections for the power and signal cable. The whole module is fixed on two base strips for stability. Figure 3.1 illustrates the arrangement of these components. A pixel module consists of 16 ROCs, which in turn consist of 52×80, thus 4160, pixels. The sensor is 285 μm thick and a pixel has a size of $100 \times 150\,\mu\mathrm{m}^2$.

A rough description of the readout of the induced charge in the sensor goes as following: Via the indium bump bond is the charge collected in the pixel transfered to the pixel unit cell (PUC), where it is preamplified and shaped. On the ROC 26 digital to analog converters (DAC) are situated with which the signal can be tuned, see Figure 3.2. Through the DAC Vana can also a calibration pulse be injected into the system, which can be delayed by the CalDel DAC. The signal is then compared to a threshold VthrComp DAC for which additionally for each pixel four trim-bits are available to get a more homogeneous threshold distribution. A signal exceeding the threshold goes to a sample and hold capacitor. In between the signal can also be changed by the Vsf DAC. When the readout is triggered the sample and hold capacitor is read out along with the pixel address and analog pulse height and the information is passed on to the double column periphery [6].

As its name suggests is the data of two columns processed in the double column

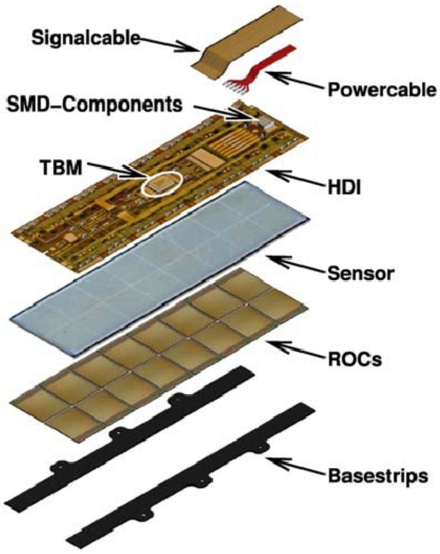

Figure 3.1: Exploded view of a module [4]

periphery. When a hit is detected in a pixel the PUC sends a signal to the timestamp buffer to store the time of the hit. Then the double column periphery reads out subsequently all pixels which were hit for the whole double column. With this only hit pixels are read out. This data is stored until in case of positive trigger decision of the Level-1 trigger the data taking is stopped and read out. If there is no trigger signal, the data will be overwritten and lost. Up to 12 timestamps and 32 hits can be buffered per double column before this happens [6].

3.2 The Examined Modules

The eight modules that were examined in the scope of this work are all from layer 3 of the pixel detector. Their exact position can be found in Table 3.1. As mentioned in chapter 1 seven of the eight modules, M0008, M0009, M0010, M0012, M0018, M0020 and M0021 had to be replaced because they are using an older version of the read out chip, where their double column periphery buffers would get corrupted and the readout would continue to loop over the buffer thus giving infinite readouts. They would get stuck in this mode with a probability increasing with particle fluence so much that they had to be turned off as they were blocking the read out of the other modules in the ladder. As for M0306, it had to be replaced as it was not responding to control signals anymore. This behavior continued for all of the tests in this work. A measurement of the leakage current is nonetheless possible as it does not need a working readout mechanism.

With irradiation the lattice structure of the silicon becomes disrupted and defects are created. This causes charge traps in the sensor, thus a charge collection deficiency, and a higher leakage current [7]. The defects can travel and dissolve themselves or can cause more damage to the structure. These processes are called

Module	r [cm]	x [cm]	y [cm]	ϕ [rad]	z [cm]	η
M0008	10.39	10.36	0.78	0.07	-10.05	-0.8579
M0009	10.39	10.13	-2.31	-0.22	-10.05	-0.8579
M0010	10.39	9.67	3.80	0.37	-3.34	-0.3156
M0012	10.39	10.36	0.78	0.07	3.34	0.3156
M0018	10.39	10.36	0.78	0.07	-23.35	-1.5486
M0020	10.39	10.36	0.78	0.07	16.68	1.2513
M0021	10.39	10.36	0.78	0.07	-3.34	-0.3156
M0306	10.39	3.06	9.93	1.27	10.05	0.8579

Table 3.1: The positions of the eight modules

annealing. First the positive annealing takes place, where the sensor properties improve, then negative annealing takes place. This process is temperature dependent, which is why the modules are stored at 5 $^{\circ}$C to keep the negative annealing to a minimum. Because of the increase in leakage current due to radiation and because the leakage current is highly temperature dependent (more detail in chapter 5) the tests are performed at -10 $^{\circ}$C.

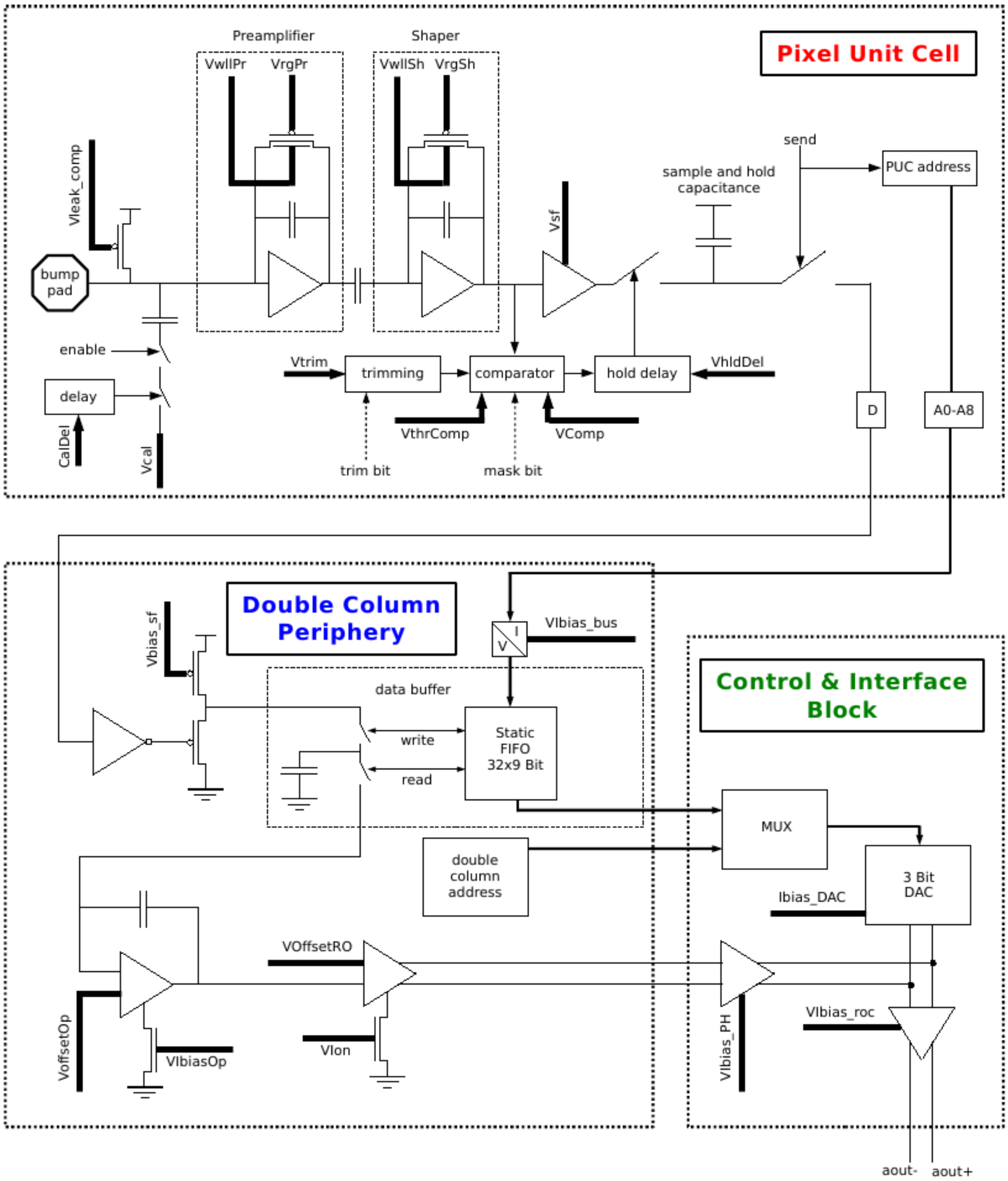

Figure 3.2: Scheme of the pixel unit cell (PUC), the double column periphery and the control & interface block [5]

4 DAC Parameters

As mentioned in chapter 3 there are 26 digital to analog converter (DAC) controlling the signal by changing a voltage. Some of them are adjusted for all ROC whereas some are adjusted for each PUC separately. The optimization of these DAC parameters for optimal readout was conducted in 2008 prior to the modules installment and again for this work after irradiation. In the following a description of the test setup, the change in the reference voltage to which the DACs voltage is compared to and the comparison of the two tests is given.

4.1 The Band Gap Reference Voltage

One of the main reasons for the changes in the DAC parameters is the change with radiation of the band gap reference voltage V_{ref} to which all voltages are compared. To quantify this change in units of DACs, two things have to be known: First is that the voltage changes linearly with the DACs set, such that a change in voltage directly translates to a change in DAC units. This is shown in 4.1a. Secondly the amount of the shift of V_{ref} has to be known. A rough estimate from 4.1b gives $\delta V_{ref}/V_{ref}$ to be approximately 1%. (Isn't 10^{-10} Gy/cm^2 a bit too low? That would be less than 0.1%)

Using

$$Vana(VanaDAC)_{Irrad} = \left(1 + \frac{\delta V_{ref}}{V_{ref}}\right) Vana(VanaDAC)_{Unirrad} \tag{4.1}$$

from [8], where $VanaDAC$ is the analog voltage in units of DACs, a change of 1% in voltage directly translates into a shift of 1% of $Vana$ in DAC units. The same holds for every DAC that is tuned and compared to the reference voltage.

4.2 Test Setup

For the optimization of the parameters of the readout electronics of the modules at -10 °C a coldbox, the red box in Figure 4.2, was used to control the temperature and humidity. The modules, each fixed to an aluminum holder, are placed on a base plate that is cooled by 4 Peltier elements. The light tight and insulating lid is closed during testing. The modules are connected to the module adapters which are in turn connected to the testboards. These testboards are connected to 4 cables: Ground, power, high voltage and via USB cables to a computer. The whole setup with the coldbox, the testboards, the high voltage power supply and the psi46expert

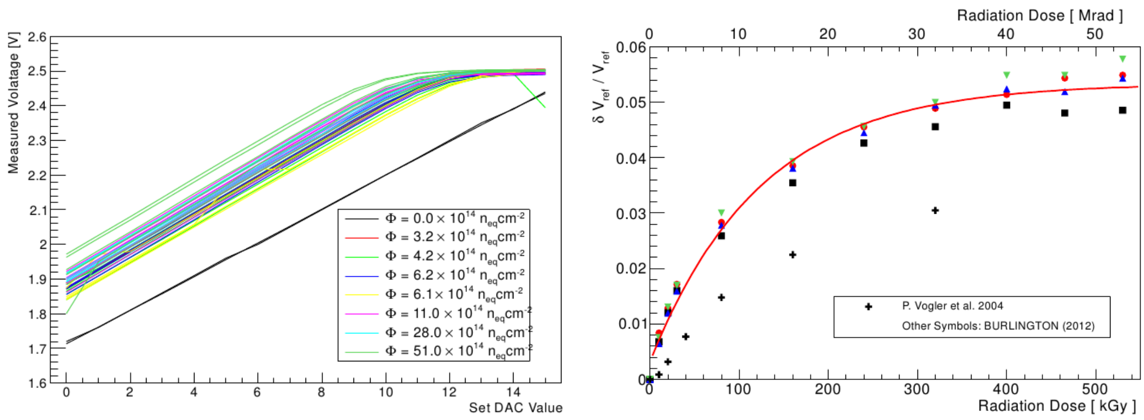

(a) (b)

Figure 4.1: (a) shows the linear behavior of the DAC value versus the DAC voltage [9]. (b) shows the expected change in the reference voltage due to radiation [10]

client [11], which conducts all necessary tests, are controlled by the elComandante software [12].

4.3 Change of the DAC Parameters

For the test procedure of 2008 before installment the following DACs are tuned:

- CalDel
- Vtrim
- VIbias_DAC
- VOffsetOp
- Vana
- VcThr
- Vsf
- VIbias_PH

In the following the tuned DACs function will be explained and their behavior after radiation discussed. A more detailed explanation of each DAC parameters can be found in [5].

CalDel This DAC is used to delay the Vcal signal, which can be used to inject a test signal into the readout mechanism as shown in Figure 3.2. CalDel is set in the VthrComp-CalDel optimization during which a stable working point is determined by injecting 5 test signals. On average it is unchanged as visible in Figure 4.3a.

Vtrim The DAC Vtrim is used to adjust the signal threshold for all pixels in a ROC to a global value. Figure 4.3b shows that it is unchanged on average compared to 2008.

Figure 4.2: The coldbox with three modules, module adapters and testboards.

Vana This DAC is set such that the analog current drawn per ROC is 24 mA. It is expected to change with irradiation because the reference voltage changes with irradiation. From Equation 4.1 a 1% shift down is expected. In Figure 4.4a a shift of 4% is observed. The discrepancy of 3% might be explained by the fact that the test structures, single ROCs in this case, used for the results in Figure 4.1b were unpowered and no bias voltage was applied to them. In [8] it was shown that the change $\frac{\delta V_{ref}}{V_{ref}}$ is larger if the structure is powered.

The height of the analog signal coming out at the end of the ROC is typically referred to as pulse height (PH). Its change with Vana is called the pulse height curve. It is optimized by tuning 3 parameters: VOffsetOp, VIbias_PH and Vsf. The goal of this procedure is to maximize the range where the dependence of the pulse height on the Vcal value is linear as shown in Figure 4.5.

VOffsetOp Changing VOffsetOp shifts the PH curve, three examples for VOffsetOp =0, 80, 160 are shown in Figure 4.6a,b,c, and search for the longest linear range in Figure 4.6d. As this is the first DAC that is worked on in the optimization the observed shift of 37% in Figure 4.4b strongly suggests that the

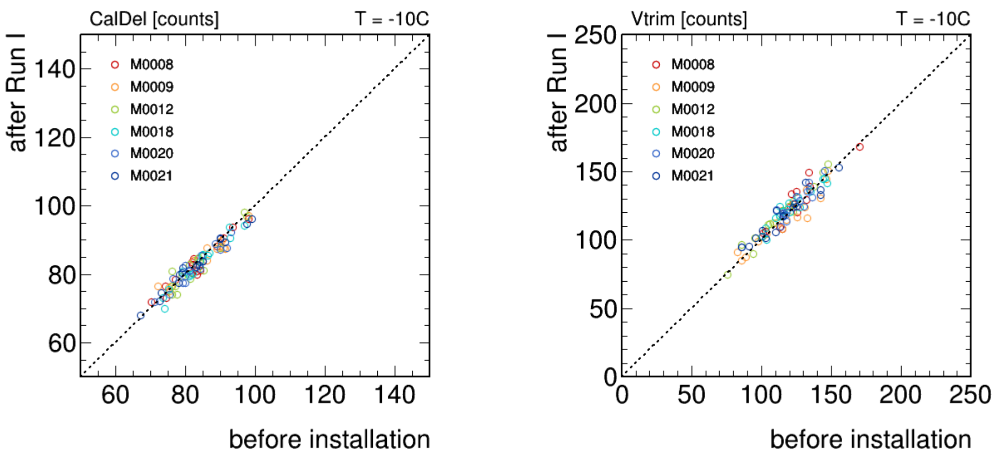

(a) (b)

Figure 4.3: The comparison of the tuned DAC parameters from the data of 2008 and 2014. CalDel and Vtrim are on average unchanged.

algorithm was changed somewhere during the 8 years time difference, because the size of the shift is not explicable with radiation damage alone.

VIbias_PH The steepness of the PH curve is adjusted with VIbias_PH as shown in Figure 4.7. The change of 49% (Figure 4.8a) is most probably also due to the fact that the algorithm changed, i.e. that VOffsetOp was already set differently.

Vsf is used to optimize linearity of PH in low Vcal range but it also affects the digital current. The optimization stops when $p_1 < 1.4$ or $I_{dig} > 5\mu$A, where p_1 is defined in the hyperbolic tangent fit function $y = p_3 + p_2 \cdot tanh(p_0 \cdot x - p_1)$. For this DAC an average shift of 2% (Figure 4.8b) was observed. Because the other two previously optimized DAC parameters VOffsetOp and VIbias_PH were already tuned differently, no definitive conclusion can be made of the radiation effect on Vsf.

VcThr(=VthrComp) This is the signal threshold defined per ROC for a fixed amplitude in Vcal units = 60. A shift of 9% is observed (Figure 4.8c).

VIbias_DAC This DAC is used to adjust the lowest address level in the ADC range, the ultrablack level (UBL), of all ROCs to the TBM's UBL. The same UBL was set but still different values are obtained for VIbias_DAC with a shift of 36% compared to the settings in 2008. This change is not yet understood.

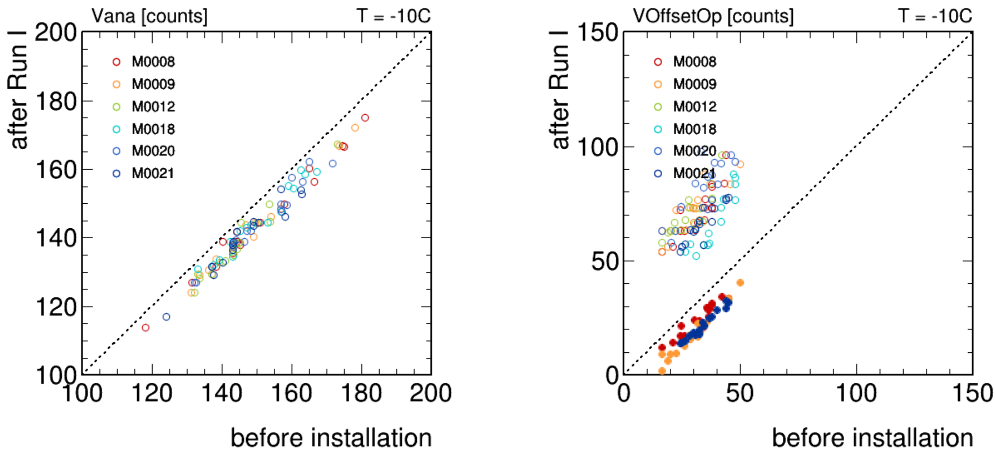

(a) (b) VOffsetOp

Figure 4.4: The comparison of the tuned DAC parameters from the data of 2008 and 2014.

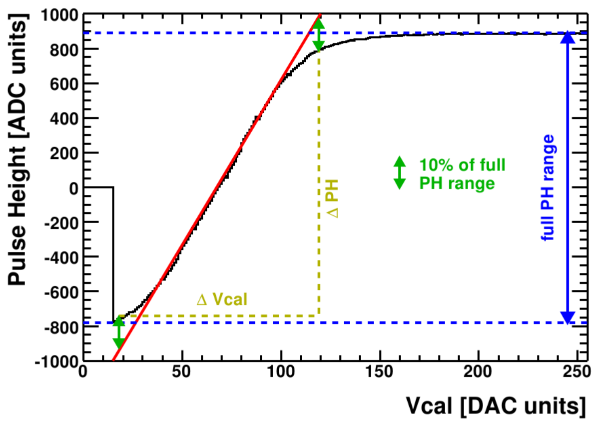

Figure 4.5: Pulse height curve [5]

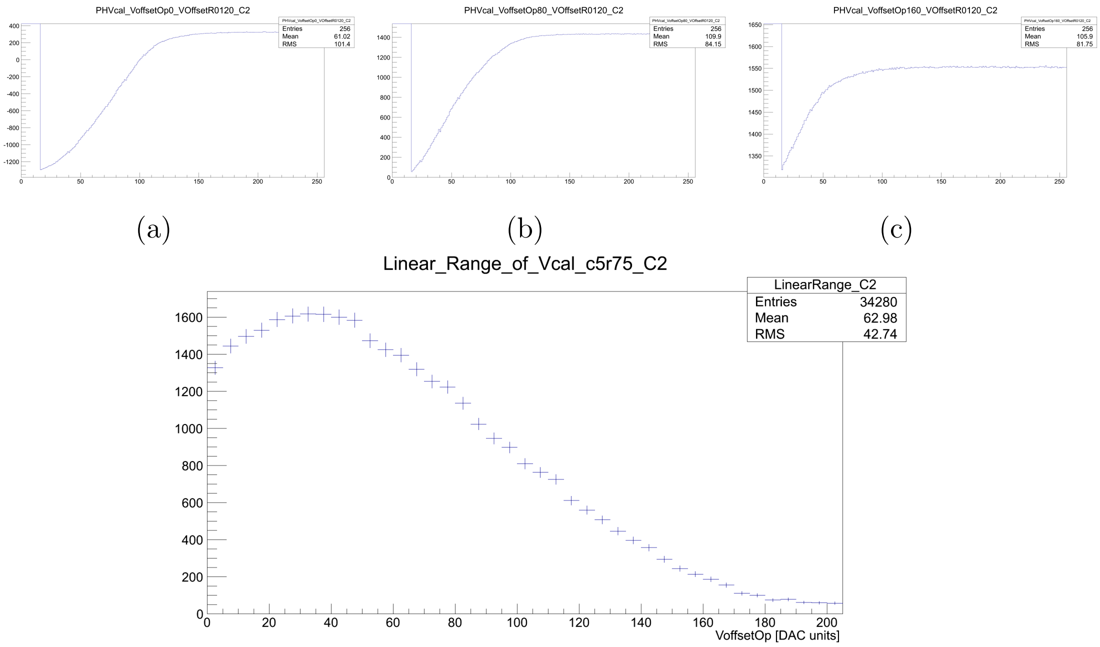

(a) (b) (c)

(d)

Figure 4.6: VOffsetOp optimization procedure: (a)-(c) The linear range is obtained form a fit for different values of VOffsetOp, three examples are shown for VOffsetOp = 0; 80; 160.
(d)The linear range is then plotted as function of VOffsetOp and the position of the maximum linear range is chosen as the optimum value for VOffsetOp.

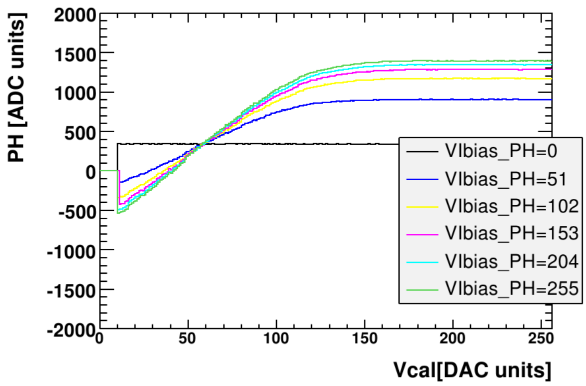

Figure 4.7: The behavior of the pulse height curve for different values of VIbias_PH [5].

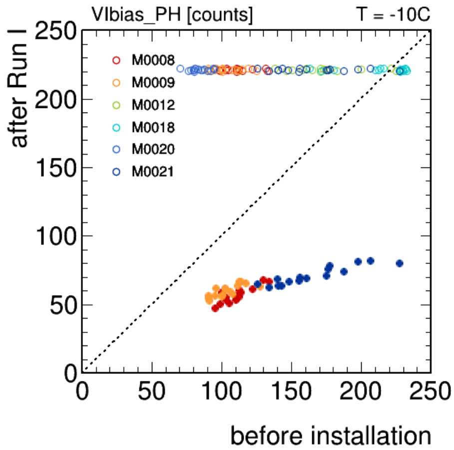

(a)

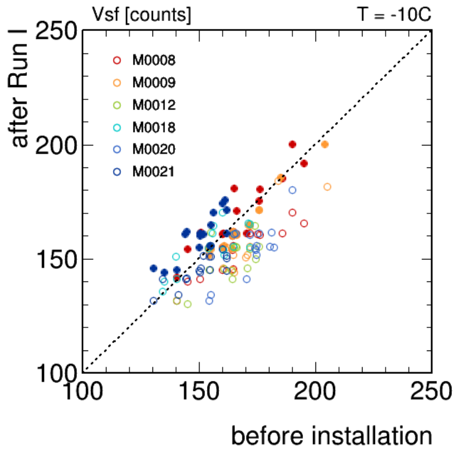

(b) Vsf

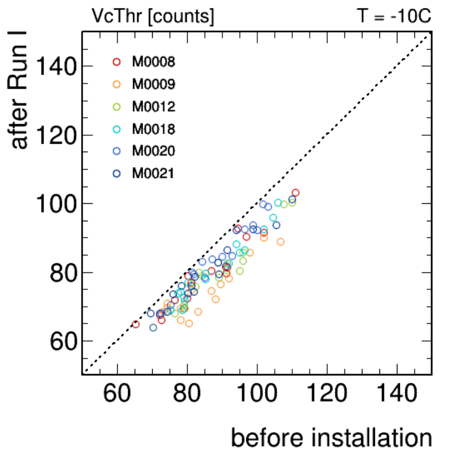

(c) VthrComp

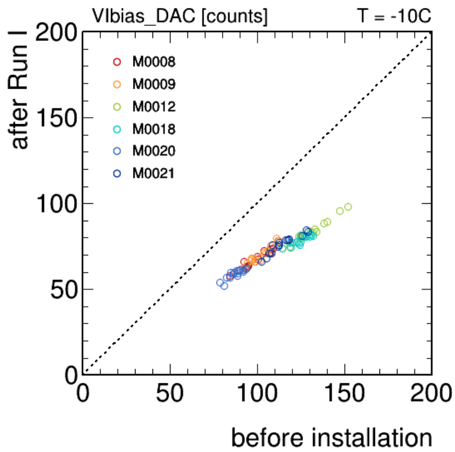

(d) VIbias_DAC

Figure 4.8: The comparison of the tuned DAC parameters from the data of 2008 and 2014.

5 Leakage Current and Current Related Damage Rate

The leakage current is a good indicator of how much radiation the sensor was subjected to. Together with the fluence the current related damage rate α can be calculated to be:

$$\alpha = \frac{\Delta I_R}{\Phi_{eq} \cdot N_{fb} \cdot V},$$

where V is the volume of the sensor and Φ_{eq} is the 1 MeV neutron fluence equivalent given in table Table 5.1 and N_{fb}, the integrated luminosity, which consists of 6.1 fb^{-1} at 7 TeV and 23.3fb^{-1} at 8 TeV. The values of th fluences are given by the FLUKA simulation, which is a fully integrated particle physics MonteCarlo simulation package [13]. Because the calculation of the fluence at 8 TeV was not available, the value at 8 TeV have to be multiplied by the ratio of the cross section at their corresponding energies $\frac{\sigma_{8\,\mathrm{TeV}}}{\sigma_{7\,\mathrm{TeV}}} = \frac{74.7\,\mathrm{mb}}{72.9\,\mathrm{mb}}$ which results in $N_{fb} = 30\,\mathrm{fb}^{-1}$. The quantity ΔI_R is the difference between the original current in 2008 and 2014 after irradiation. As they were measured at $T = -10^{\circ}\,\mathrm{C}$, they are recalculated to the reference temperature of $T_R = 20^{\circ}\,\mathrm{C}$ as following:

$$\Delta I_R = \Delta I \cdot R,$$

with

$$R = \left(\frac{T_R}{T}\right)^2 exp\left(-\frac{E_g}{2k_B}\left[\frac{1}{T_R} - \frac{1}{T}\right]\right) = 15.54,$$

where $E_g = 1.12\,\mathrm{eV}$ is the bandgap. The factor R shows clearly the strong temperature dependence of the leakage current. Thus environmental temperature has to be well defined. A difference in temperature up to $1.9\,^{\circ}\mathrm{C}$ has been observed between powered and unpowered modules [14]. Thus for the leakage current measurement the modules are not powered.

The error on the leakage current measurement was assumed to be $2\,\mu\mathrm{A}$ or approximately 10%, as repeated measurements showed. A further error source comes from the binning and general statistical fluctuations on the fluence, that are taken into account by the errors given by FLUKA. They are listed in Table 5.1. They correspond to an approximately 1% error on the fluence. The off-centered beam spot was not taken into account but because the binning of FLUKA is already quite coarse, the effect is of the order of 1% or less, thus it was neglected here. The last error source is the uncertainty on the temperature. In [14] a good homogeneity along the module position in the coldbox base plate was shown at -25 $^{\circ}\mathrm{C}$. Based on the measurements from this work a conservative uncertainty of $1\,^{\circ}\mathrm{C}$ was assumed on the temperature. This was then used to calculate the uncertainty on R, the recalculation factor. This

Module	η	I_{ini} [μA]	I [μA]	I_R [μA]	$\Phi_{eq} \cdot 10^{11}$ [cm^{-2}fb^{-1}]	$\alpha \cdot 10^{-17}$ [A/cm]
M0008	-0.8579	0.047	17.99	278.8	7.923 ± 0.090	$3.923 ^{+0.381}_{-0.424}$
M0009	-0.8579	0.036	16.96	262.9	7.923 ± 0.090	$3.700 ^{+0.359}_{-0.400}$
M0010	-0.3156	0.023	19.58	303.8	7.908 ± 0.090	$4.284 ^{+0.415}_{-0.463}$
M0012	0.3156	0.031	18.36	284.8	7.884 ± 0.076	$4.027 ^{+0.390}_{-0.434}$
M0018	-1.5486	0.026	15.93	247.1	8.064 ± 0.089	$3.417 ^{+0.332}_{-0.369}$
M0020	1.2513	0.009	17.08	265.2	8.106 ± 0.082	$3.648 ^{+0.354}_{-0.394}$
M0021	-0.3156	0.253	20.02	307.1	7.908 ± 0.089	$4.330 ^{+0.420}_{-0.466}$
M0306	0.8579	0.100	18.26	274.7	7.916 ± 0.066	$3.869 ^{+0.374}_{-0.417}$

Table 5.1: The input values for the calculation of α and its result

gives an $R_{minus} = 14.04$ for -9 °C and an $R_{plus} = 17.20$ for -11 °C, or an error of approximately 10%.

The resulting values for α can be found in Table 5.1. In order to visualize the dependence of α on the pseudo rapidity η , the results are also plotted in Figure 5.1. The red line correspond to a fit with a constant which is equivalent to the mean current related damage rate

$$\alpha_{mean} = 3.86 \pm 0.14 \cdot 10^{-17} [\text{A/cm}].$$

Assuming an ambient annealing temperature of approximately 21 °C this mean value corresponds to approximately 1 month of annealing time according to Figure 5.2, which is in good agreement with the rough range estimation from 3 weeks to 8 weeks. But for the individual modules an η dependence is visible, even though the fluence values do take into account that at higher η position the particle path in the sensor is longer, thus doing more damage. This becomes especially visible in Figure 5.3, where α_{mean} was used to calculate the fluence by rearranging the equation for α such that $\Phi_{eq} = \frac{I_R}{\alpha_{mean} N_{fb} V}$. The so obtained values for Φ_{eq} show the same behavior with η as they linearly depend on the leakage current. The increasing fluence with increasing $|\eta|$ is contradiction with the FLUKA simulation, but, as it still lies within the errors, no conclusion about this can be drawn.

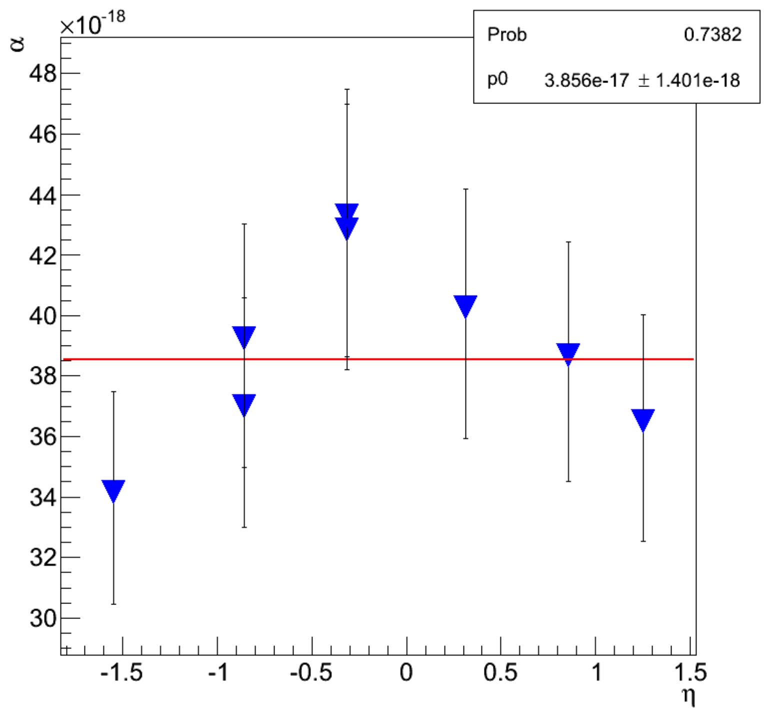

Figure 5.1: The current related damage rate α as a function of η

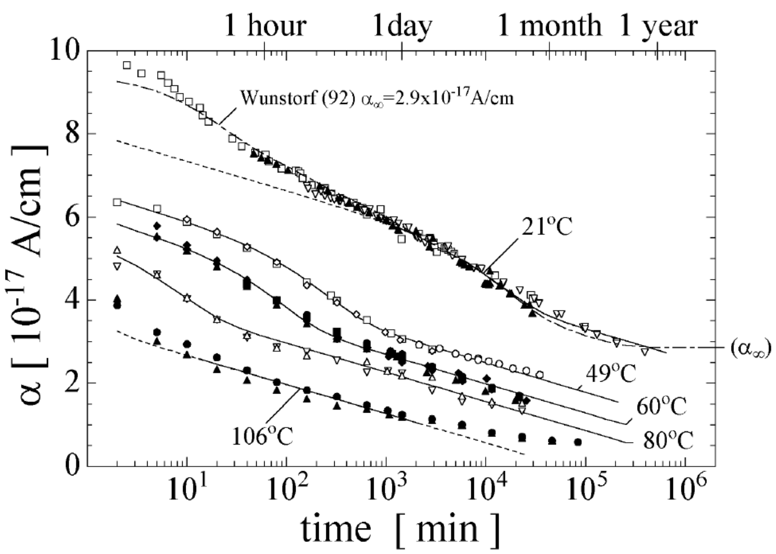

Figure 5.2: α versus the annealing time for different annealing temperatures [7]

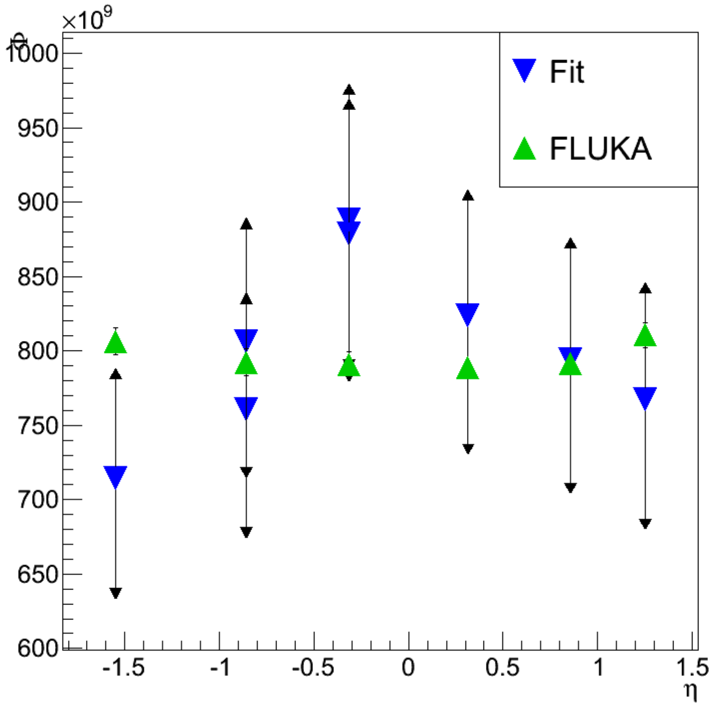

Figure 5.3: Recalculated fluence from $\Phi_{eq} = \frac{I_R}{\alpha_{mean} N_{fb} V}$ and the values from the FLUKA simulation as a function of η

6 VCal Calibration

The method used in this work to determine how many e^- correspond to a VCal unit is the pulse height method. For this charge is induced by a monochromatic X-ray source and the distribution of the pulse height is read out and fitted to determine the mean. This was done for four different targets which induce a different amount of charge in the sensor, thus resulting in four mean values. The correlation between expected charge deposition from the four targets and the mean pulse height values in VCal units are fitted with a linear function. The slope of this function corresponds to the amount of e^- per unit of VCal. These values are to be compared to the original calibration done in 2008. But it is important to be aware that in 2008 the calibration was done using the threshold method, which was shown to give at least up to $16\,e^-$/VCal less than the calibration done using the PH method [6]. For the calibration with the threshold method the comparator threshold is varied by means of the VthrComp DAC and the number of signals above it is read out. The resulting distribution is then fitted with an error function and the 50% point of the plateau used for the VCal determination.

6.1 X-Ray Setup

For the VCal calibration the X-ray box was used. Like in the coldbox setup, the modules are fixed on a baseplate which is cooled with Peltier elements, in a light-tight box. Above this the X-ray source is fixed with the different targets to the left of it.

The four targets used are Molybdenum (Mo), Silver (Ag), Tinn (Sn) and Barium (Ba). Table 6.1 lists the amount of electrons created in the sensor for the different targets. These values will be used on the y-axis for the fit of the slope.

Target	E_{K_α}	N_{e^-}
Mo	17479.372	4855
Ag	22162.917	6156
Sn	25271.36	7019
Ba	32193.262	8942

Table 6.1: The transition line K_α [15] and the number of created electrons for each of the used targets

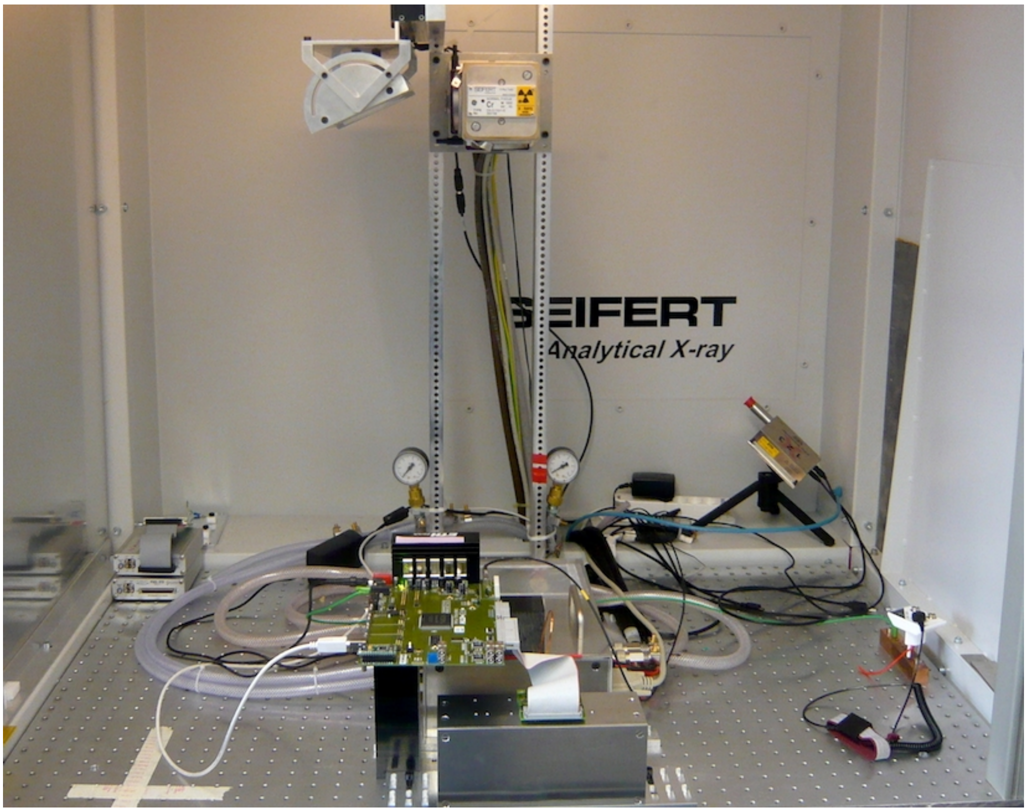

Figure 6.1: Picture of the test setup in the X-ray box.

6.2 Vcal Calibration

To ascertain correct readout the VCal calibration is done using the DAC parameters resulting from the optimization in the coldbox. Furthermore was the trim and pulse height optimization performed again. Data were taken with a random trigger at $\tilde{3}1$ kHz with a data acquisition time was 12 seconds to maximally use the available RAM on the testboard. In order to get enough statistics for all targets the measurements were repeated 3, 3, 4 and 6 times for Mo, Ag, Sn and Ba respectively. The reason for the low statistics for the Barium sample is that the sensor is almost transparent to the this wavelength resulting in a approximately uniform probability along the sensor thickness for the charge deposition. And if the charge is deposited lower in the sensor, spread of the charge to neighboring pixels (charge sharing) becomes more of a problem as the background events arising from pixels containing only a fraction of the total charge deposition will increase which is nicely visible in Figure 6.2d.

These background events lie mainly on the left of the signal peak, which is assumed to be gaussian. Because of this an asymmetric fit range was chosen to accommodate the asymmetric background. In more detail: First a gaussian is fitted over the whole range and the peak position of this gaussian $+25$ is taken as the initial guess $m_{initial}$ for the position of the signal peak. The fit range is then [$m_{initial}$-10, $m_{initial}$+50].

For the data obtained for this study this function fitted all the distributions well. But a more detailed study to optimize the fits would be needed to give reasoning to these values. A more complex function by Paul Turner that attempts to also fit the whole background did not give better fits to the signal peaks, which was also visible by the fact that the spread of the measured slopes was broader. In Figure 6.2 some resulting histograms and fits in red are shown for the different targets.

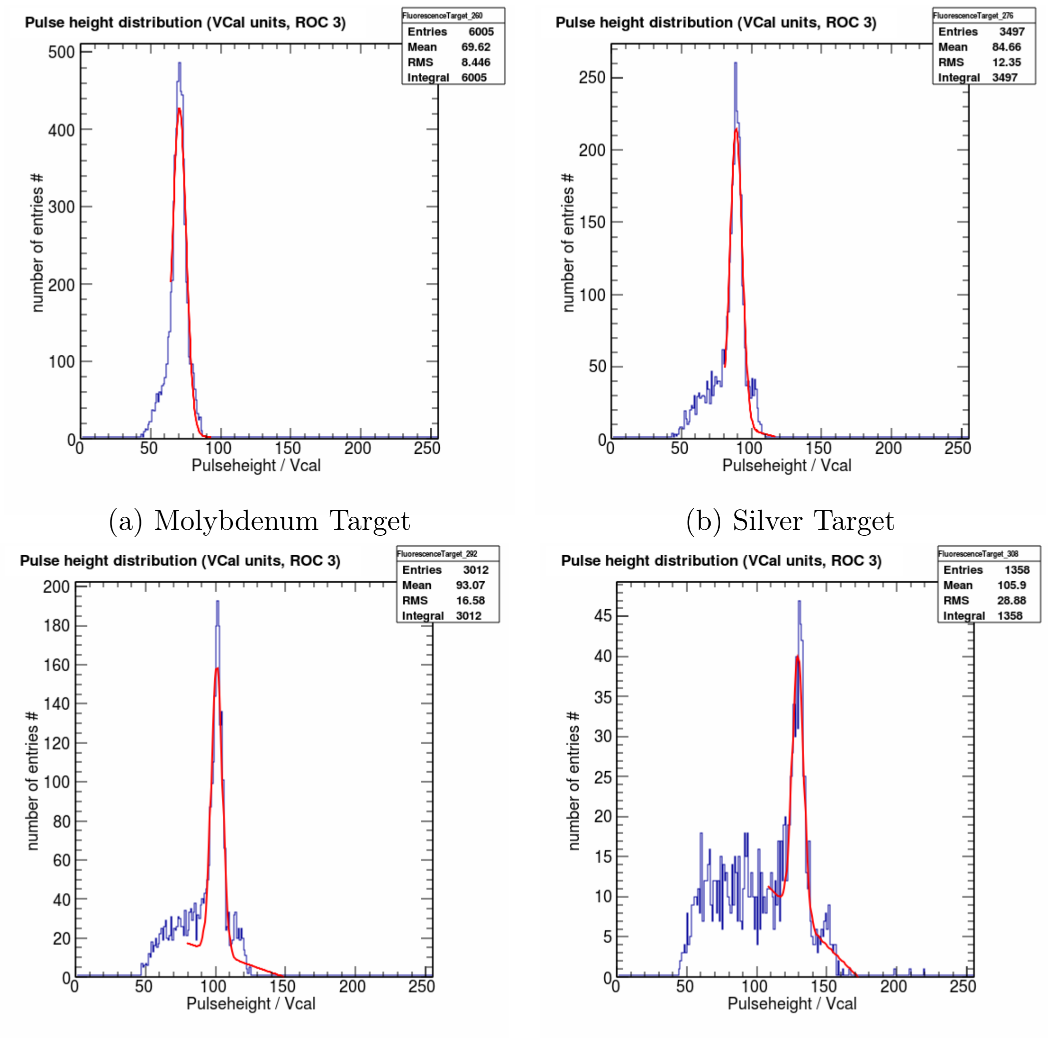

(a) Molybdenum Target

(b) Silver Target

(c) Tinn Target

(d) Barium Target

Figure 6.2: The pulse height distributions for the different targets for ROC3 of M0018

6.3 Reproducibility of the VCal Calibration

To ascertain that the VCal calibration using the PH method are reproducible 5 consecutive measurements, which will be referred to as runs, with the 4 X-ray targets

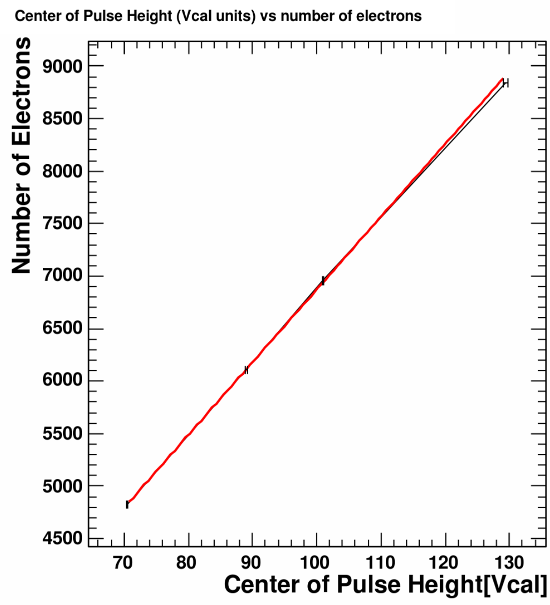

Figure 6.3: The linear fit (red line) to the four target mean positions for ROC3 of M0018

were conducted for module M0009 and M0021. Out of the 5 runs for M0021 two had to be discarded as the Barium distribution for those runs showed much too low statistics. For each ROC of each module the mean of the runs was calculated and the value per run divided by the mean of all runs was plotted on the left in Figure 6.4 and Figure 6.5. On the right of these figures on can see the distribution on the left side multiplied by the total mean of all ROCs. The RMS of this distribution is a measure for the reproducibility of the calibration. With $RMS = 0.76 \pm 0.06$ for M0009 and $RMS = 1.27 \pm 0.13$ for M0021 a good reproducibility was achieved.

These runs were conducted without replacing the modules in the X-ray box in between. A comparison with the values obtained 2 weeks prior to the reproducibility measurements is shown in Table 6.2. It clearly shows that, even tough M0009 showed a better reproducibility than M0021, the difference between the two sets of measurements 2 weeks apart is larger. Especially the difference for ROC 15 of $12.17\,\mathrm{e}^-/\mathrm{VCal}$ is huge compared to the RMS of the reproducibility test of 0.76. This is even though the distribution for the different targets as well as the fit are well behaved. One explanation might be that the two sets of measurements two weeks apart use different calibrations of the DAC parameters, pulse height and trimming. Thus it has so be concluded that per ROC large differences of the order of $12\,\mathrm{e}^-/\mathrm{VCal}$ can occur, but the mean of all ROCs seems to be not as prone to changes in the module holder placement as the ROCs. Further measurements are needed to achieve a significant measure of the reproducibility.

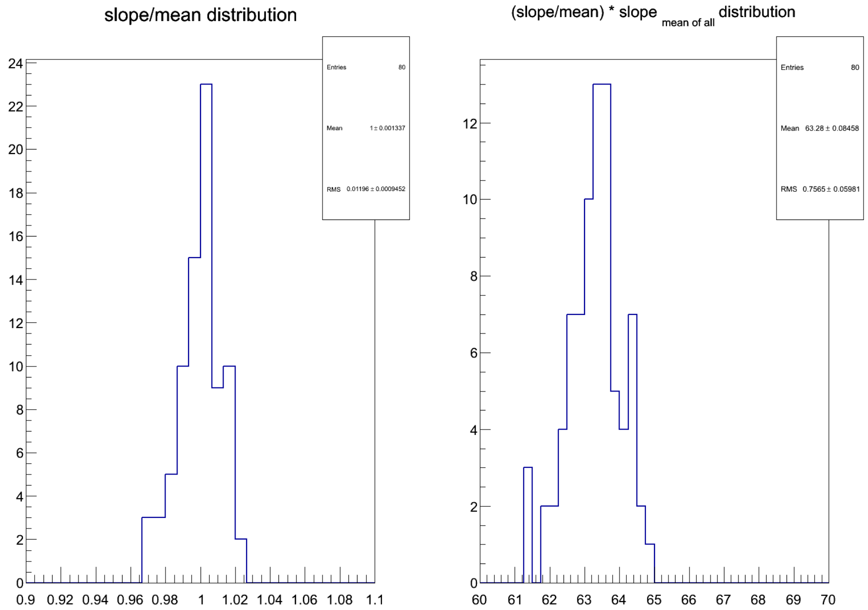

Figure 6.4: Reproducibility test for M0009

6.4 Comparison with 2008 Measurements

Unfortunately the data from 2008 only contains the average of all ROCs per module. Thus even lower statistics are available as only 6 of the 8 modules were still functioning properly in 2014. The data is shown in Table 6.3. A mean difference of 17.7 e^-/VCal or 29.7% was observed.

Figure 6.7 shows the comparison of the fit for 4 and 3 fluorescence targets. The distribution of the slopes has a smaller rms of 10.6 for 4 targets compared to the rms of 13.0 for 3 targets. Thus the values with 4 X-ray targets are used for the comparison with the 2008 measurements.

The mean and rms of the distribution of the slopes and offsets per ROC can further be compared to the distributions measured in 2008 shown in Figure 6.6. The comparison of these values is summarized in Table 6.4.

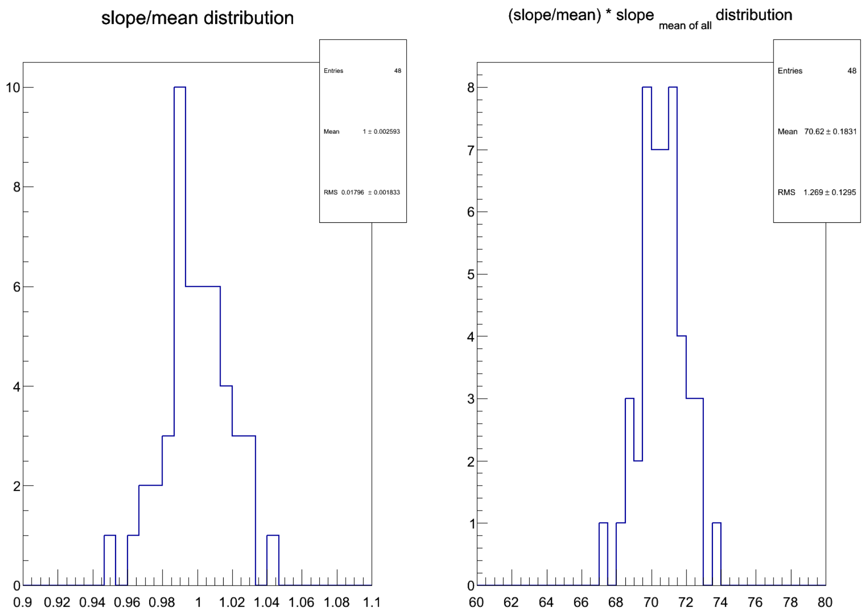

Figure 6.5: Reproducibility test for M0021

	M0009 mean	M0009 2 weeks prior	Difference	M0021 mean	M0021 2 weeks prior	Difference
Mean(ROCs)	63.28	67.51	4.23	70.62	72.77	2.16
ROC0	69.43	76.00	6.58	65.81	64.92	-0.89
ROC1	63.31	65.82	2.51	61.94	62.10	0.16
ROC2	64.86	70.67	5.82	77.32	80.69	3.37
ROC3	65.94	66.33	0.38	63.03	79.33	16.30
ROC4	66.03	68.98	2.95	79.26	74.07	-5.19
ROC5	64.37	65.76	1.39	73.81	67.78	-6.03
ROC6	65.04	68.76	3.73	60.69	69.30	8.61
ROC7	63.20	65.65	2.45	77.46	70.53	-6.92
ROC8	64.04	69.10	5.06	78.12	76.98	-1.14
ROC9	58.64	66.19	7.55	76.79	81.76	4.96
ROC10	60.90	65.01	4.11	70.10	74.36	4.25
ROC11	62.64	62.63	-0.01	63.81	63.57	-0.25
ROC12	59.16	61.65	2.48	64.04	70.07	6.03
ROC13	60.08	69.99	9.91	69.32	79.01	9.69
ROC14	64.51	65.13	0.62	71.33	75.94	4.62
ROC15	60.32	72.48	12.17	77.06	73.99	-3.06

Table 6.2: The data obtained for the reproducibility measurements

	2008	2014	2014-2008	Difference [%]
M0008	60 e^-/VCal	84.3 ± 8.4 e^-/Vcal	24.3	40.5
M0009	62 e^-/VCal	67.5 ± 3.6 e^-/Vcal	5.5	8.9
M0010	59 e^-/VCal	–	–	–
M0012	62 e^-/VCal	81.3 ± 6.6 e^-/Vcal	19.3	31.1
M0018	58 e^-/VCal	69.9 ± 5.5 e^-/Vcal	11.9	20.5
M0020	59 e^-/VCal	89.5 ± 10.2 e^-/Vcal	30.5	51.7
M0021	58 e^-/VCal	72.8 ± 6.0 e^-/Vcal	14.8	25.5
M0306	69 e^-/VCal	–	–	–

Table 6.3: Comparison of the 2008 and 2014 data. The errors given are the RMS of all ROCs.

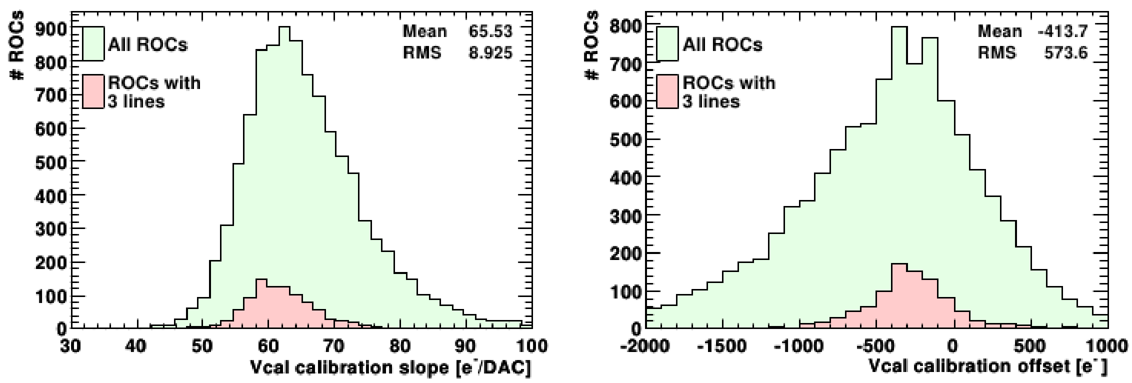

Figure 6.6: The slope and offset distribution for all tested modules in 2008 [16]

	2008	2014	Difference	Difference [%]
Mean ± rms	65.5 ± 8.9	77.6 ± 10.6	12.1	18.4
Offset ± rms	-414 ± 574	-1215 ± 946	801	294

Table 6.4: Comparison of the 2008 and 2014 data.

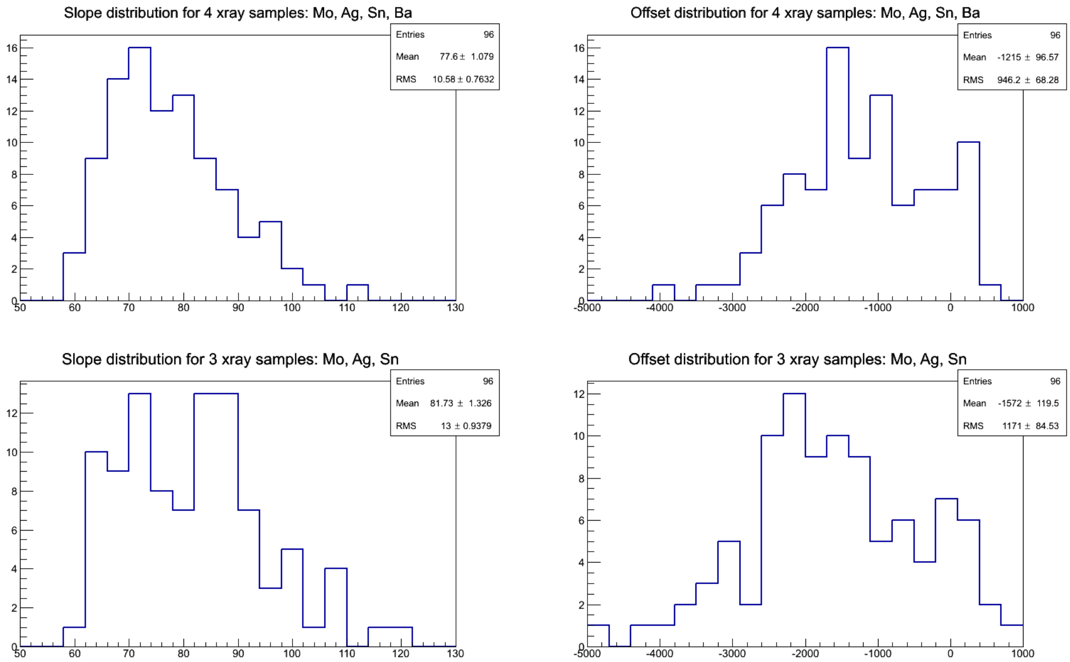

Figure 6.7: The slope and offset distribution for the 6 tested modules (16 ROCs each) for 4 and 3 fluorescence targets

7 Conclusions

The eight pixel modules were tested in 2008 prior to their installment in the CMS detector. Then $30\,\mathrm{fb}^{-1}$, or approximately $2.4 \cdot 10^{13} \frac{1}{\mathrm{cm}^2}$ 1 MeV neutron equivalent fluence, were collected and the eight modules were extracted from the detector. For this thesis they were retested and the two data sets compared.

The shift of the DAC parameter Vana by 4% is bigger than what is expected by the radiation damage done to the reference voltage, which is about 1%. But it might be explained by the fact that the environments for the two test were different as the modules were powered and biased during the whole time of irradiation. For CalDel and Vtrim on average no shift was observed. The PH curve calibration parameters VOffsetOp, VIbias_PH and Vsf changed mainly due to the fact that the algorithm probably was changed between the two calibration done in 2008 and 2014. The shifts of VthrComp and VIbias_DAC still needs some investigation into the tuning procedure.

The calculated mean current related damage rate

$$\alpha_{mean} = 3.86 \pm 0.14 \cdot 10^{-17}\mathrm{A/cm}$$

corresponding to approximately 1 month of annealing at $21\,^\circ\mathrm{C}$ lies withing the expected range.

For the VCal calibration an increase of the mean slope from 65.53 in 2008 to $77.6\,\mathrm{e}^-/\mathrm{VCal}$ or a increase of 18.42% was observed. Though it has to be noted that the two calibrations done in 2008 and 2014 were conducted with different techniques, with the threshold and pulse height method respectively. Differences in the test environment like temperature and calibration procedures could contribute to this.

A Bibliography

[1] Cern website. ONLINE. URL http://public.web.cern.ch/public. Accessed: 2014, June 13.

[2] Cms website. ONLINE. URL http://cms.web.cern.ch/news/how-cms-detects-particles. Accessed: 2014, June 13.

[3] G.L. Bayatian et al. Cms physics technical design report, volume i: Detector performance and software. Technical report, CERN, 2006.

[4] C. Eggel. *CMS Pixel Module Qualification and Search for* $B_s^0 \to \mu^+\mu^-$. PhD thesis, ETH Zürich, 2009.

[5] S. Dambach. *CMS Pixel Module Readout Optimization and Study of the* B^0 *Lifetime in the Semileptonic Decay Mode*. PhD thesis, ETH Zürich, 2009.

[6] J. Hoß. X-ray calibration of pixel detector modules for the phase i upgrade of the cms experiment. Master's thesis, Karlsruher Institut für Technologie, 2012.

[7] M. Moll. *Radiation Damage in Silicon Particle Detectors*. PhD thesis, Universität Hamburg, 1999.

[8] L. Hoppenau. Characterization of the analog and digital cms pixel readout chip after irradiation. Master's thesis, ETH Zürich, 2013.

[9] T. Rohe et al. Radiation hardness of cms pixel barrel modules. *Nucl. Instr. and Methods in Pyhsics Research Section A*, 624(2), 2010.

[10] L. Hoppenau. Irradiation effects on n-type and p-type field effect transistors in a 0.25 μm technology, 2012.

[11] *CMS internal page*. URL https://twiki.cern.ch/twiki/bin/viewauth/CMS/Psi46Expert.

[12] *CMS internal page*. URL https://twiki.cern.ch/twiki/bin/viewauth/CMS/ElComandante.

[13] Fluka simulation homepage. ONLINE. URL http://www.fluka.org/fluka.php.

[14] S. Storz. Coldbox upgrade and commissioning and temperature analysis of pixel modules, 2014.

[15] P. Indelicato L. de Billy E. Lindroth J. Anton J.S. Coursey D.J. Schwab C. Chang R. Sukumar K. Olsen R.D. Deslattes, E.G. Kessler Jr. and R.A. Dragoset. X-ray transition energies (version 1.2). ONLINE, 2005. URL http://physics.nist.gov/XrayTrans. Accessed: 2014, June 13.

[16] P. Trüb. *CMS Pixel Module Qualification and Monte-Carlo Study of* $H \to \tau^+\tau^- \to \ell^+\ell^- \not{E}_T$. PhD thesis, ETH Zürich, 2008.